RESEARCH ARTICLE

NANO · MICRO small
www.small-journal.com

Doping Regulation Stabilizing δ-MnO_2 Cathode for High-Performance Aqueous Aluminium-ion Batteries

Shuimei Chen, Yueqi Kong, Cheng Tang, Nashaat Ahmed Gadelhak, Ashok Kumar Nanjundan,* Aijun Du, Chengzhong Yu,* and Xiaodan Huang**

δ-MnO_2 is a promising cathode material for aqueous aluminium-ion batteries (AAIBs) for its layered crystalline structure with large interlayer spacing. However, the excellent Al ion storage performance of δ-MnO_2 cathode remains elusive due to the frustrating structural collapse during the intercalation of high ionic potential Al ion species. Here, it is discovered that introducing heterogeneous metal dopants with high bond dissociation energy when bonded to oxygen can significantly reinforce the structural stability of δ-MnO_2 frameworks. This reinforcement translates to stable cycling properties and high specific capacity in AAIBs. Vanadium-doped δ-MnO_2 (V-δ-MnO_2) can deliver a high specific capacity of 518 mAh g^{-1} at 200 mA g^{-1} with remarkable cycling stability for 400 cycles and improved rate capabilities (468, 339, and 285 mAh g^{-1} at 0.5, 1, and 2 A g^{-1}, respectively), outperforming other doped δ-MnO_2 materials and the reported AAIB cathodes. Theoretical and experimental studies indicate that V doping can substantially improve the cohesive energy of δ-MnO_2 lattices, enhance their interaction with Al ion species, and increase electrical conductivity, collectively contributing to high ion storage performance. These findings provide inspiration for the development of high-performance cathodes for battery applications.

1. Introduction

Manganese dioxides (MnO_2) possess favorable characteristics as cathode materials in rechargeable batteries due to their high redox potential and the ability to undergo two-electron transfer in Mn^{4+}/Mn^{2+} reactions, resulting in high specific capacity (theoretically 616 mAh g^{-1}) and high energy density.[1–3] Among various MnO_2 polymorphs, δ-MnO_2, with its layered crystalline structure and large interlayer spaces of ≈0.7 nm, is particularly well-suited for efficient ion storage and transport in aqueous multivalent metal-ion batteries, where metal cations are usually solvated and have large sizes.[4–6] However, as a typical *3d* transition metal oxide, MnO_2 cathodes at discharge steps usually experience Mn^{3+} valence transition and undergo Jahn-Teller distortion, leading to violent structural instability and disproportion reactions that release Mn ions into electrolytes and cause battery performance degradation.[7–9]

This issue would become more severe when MnO_2-based cathodes encounter multivalent charge carriers in many post-lithium-ion battery technologies. For instance, δ-MnO_2-based materials have been recently studied as promising cathodes for aqueous aluminium-ion batteries (AAIBs), which demonstrated high initial capacities of over 550 mAh g^{-1} but experienced fast capacity fading and short cycling life (<100 cycles).[10] The theoretical study of the diffusion of Al ions within δ-MnO_2 cathodes suggested complicated Jahn-Teller distortions in the Al/MnO_2 system.[11] This can be ascribed to the multivalent nature of Al ions and their complex cations that cause substantial valence changes and alterations in the bond structures of the δ-MnO_2 hosts.[12] These highly charged ions can also induce strong coulombic interactions with the δ-MnO_2 lattice,[13]

S. Chen, Y. Kong, N. A. Gadelhak, A. K. Nanjundan, C. Yu, X. Huang
Australian Institute for Bioengineering and Nanotechnology
The University of Queensland
Brisbane, QLD 4072, Australia
E-mail: y.kong@uq.edu.au; ashok.nanjundan@unisq.edu.au; c.yu@uq.edu.au; x.huang@uq.edu.au

The ORCID identification number(s) for the author(s) of this article can be found under https://doi.org/10.1002/smll.202312229

DOI: 10.1002/smll.202312229

C. Tang, A. Du
Centre for Materials Science
School of Chemistry and Physics
Queensland University of Technology
Gardens Point Campus
Brisbane, QLD 4000, Australia

A. K. Nanjundan
Centre for Future Materials
School of Engineering
University of Southern Queensland
Springfield, QLD 4300, Australia

C. Yu
School of Chemistry and Molecular Engineering
East China Normal University
Shanghai 200241, P. R. China

leading to the collapse of crystalline lattices during battery cycling. Several reports have shown the structural transition of δ-MnO_2 cathodes from the layered birnessite phase to an amorphous state after the initial cycles.[13,14] The bond structure distortion has been identified as a crucial issue for the leaching of manganese ions into battery electrolytes, while a collapsed crystalline structure would further exacerbate this process, collectively giving rise to the dissolution of active manganese species and a subsequent decrease in capacity.

In recent studies on AAIBs, researchers have focused on optimizing the electrolyte composition to mitigate the dissolution of δ-MnO_2 cathodes. He et al. introduced manganese sulfate ($MnSO_4$) into the AAIB electrolyte to regulate the reaction balance and alleviate manganese ion leaching.[10] This approach led to improved specific capacity and discharge voltage of the δ-MnO_2 cathode. However, the cathode capacity decayed over cycling, resulting in a relatively short lifespan of only 65 cycles and limited rate capacities. Further advancements in structural engineering for cathode materials are necessary to address the capacity decay and lifespan limitations observed in δ-MnO_2-based cathodes for AAIBs.

Pre-intercalation and heteroatoms doping are recognized as effective structural engineering strategies for MnO_2-based electrodes in diverse electrical energy storage technologies including supercapacitors, alkali metal-ion batteries, and aqueous zinc-ion batteries.[8,15,16] Various cations (e.g., Li^+, Na^+, K^+, Fe^{2+}, Al^{3+}, etc.) are selected for pre-intercalation in δ-MnO_2 to regulate the interlayer environment and improve the structural stability.[4,17–19] In AAIBs research, Yan et al. and Ran et al. separately reported the preparation of Al^{3+} per-intercalated MnO_2 cathodes (Al_xMnO_2) to work with their Al alloy anodes (Zn-Al alloy and Al-Cu lamellar alloy).[13,17] The Al_xMnO_2 cathode coupled with Zn-Al alloy achieved a high initial capacity of more than 650 mAh g^{-1} at 100 mA g^{-1}, but only presented 80 cycles at the same current with a relatively low retained capacity of 460 mAh g^{-1} and a decreased rate capacity of 230 mAh g^{-1} at 1 A g^{-1}.[13] The complicated Al-Cu lamellar alloy can enable the Al_xMnO_2 cathode to run 400 charge/discharge cycles but deliver a relatively low capacity (≈480 mAh g^{-1} at 100 mA g^{-1}).[17]

Elemental doping, referring to the introduction of heteroatoms into MnO_2 lattices, is often considered as a more promising strategy to inhibit the structure distortion for stable cathode materials, because heteroatoms doping can tune the atomic and electronic structures of MnO_2.[15,16] Until now, only Geng's group recently reported cobalt (Co)-doped δ-MnO_2 nanosheets as AAIB cathode, as Co has been identified to be a highly efficient dopant for MnO_2-based cathodes in alkali metal-ion and aqueous zinc-ion batteries.[12] However, despite a high initial capacity of 585 mAh g^{-1} and a good cycling life of 300 cycles at 100 mA g^{-1}, Co-doped δ-MnO_2 appears not to have adequate long-term stability, only displaying 78% capacity retention after cycling and low rate capacities (e.g., 185 mAh g^{-1} at 500 mA g^{-1}).

Transferring know-how from other batteries doesn't seem directly practical considering the highest ionic potential (defined as the charge-to-radius ratio) of Al^{3+} ions among all reported metal ions as the primary charge carriers for rechargeable batteries.[20] The high ionic potential induces strong affinities between Al^{3+} ions and partially negatively charged oxygen sites in the δ-MnO_2 cathode, and the system encounters a violent perturbation when ions move through the lattices during battery cycling, resulting in structural degradation. Therefore, stabilizing δ-MnO_2 cathode remains particularly challenging in AAIBs for high capacity and long cycle life, calling for a revisit of the doping strategy. Heteroatom dopants having high bond dissociation energies with oxygens are recognized as "oxygen binders" in the fabrication of metal oxide thin-film transistors.[21] These dopants can strengthen the metal oxide frameworks and enhance their stabilities.[22,23] Recent studies of Ni-rich cathode materials for lithium-ion batteries have also emphasized the importance of high-bond dissociation energy dopants for structural stabilization and improved electrochemical performance.[24,25] Exploring heteroatoms doping with high bond dissociation energy in oxide environments sheds promising lights on stabilizing δ-MnO_2 cathodes for high-performance AAIBs.

To validate this hypothesis, we selected three 3*d* metal elements (Zn, V, and Ti) as model dopants and investigated their impact on the electrochemical stability and battery performance of δ-MnO_2-based cathodes in AAIBs (**Scheme 1**). Both computational simulations and experimental studies demonstrated that Ti—O and V—O bonds, with higher bond dissociation energies (662 and 644 kJ mol^{-1}) compared to Mn—O bonds (402 kJ mol^{-1}),[26] remarkably strengthen the δ-MnO_2 framework, contributing to enhanced structural stability and suppressed Mn dissolution during battery cycling. Conversely, Zn—O, with a lower bond dissociation energy (284 kJ mol^{-1}), resulted in the opposite effect. Additionally, V doping showed superior performance among Ti and V dopants, attributed to its aliovalent nature (V^{5+} vs Ti^{4+} and Mn^{4+}) and higher electronegativity, which substantially improved electrical conductivity and induced stronger affinity toward complex Al cations. V-δ-MnO_2 exhibited impressive electrochemical performance as an AAIB cathode material, delivering a high reversible capacity of 518 mAh g^{-1} with excellent cycling stability (86% capacity retention after 400 cycles) at 200 mA g^{-1} and improved rate capabilities (468, 339, and 285 mAh g^{-1} at 0.5, 1, and 2 A g^{-1}, respectively), surpassing other reported cathode materials in AAIBs.

2. Results and Discussion

2.1. Synthesis and Characterization of Pristine and Doped δ-MnO_2

Pristine δ-MnO_2 nanoflakes and the doped variants were synthesized via hydrothermal methods using manganese nitrate ($Mn(NO_3)_2$) as the precursor and specific metal salts for doping. The morphology and crystal structure of the δ-MnO_2 materials were examined using field emission scanning electron microscopy (SEM) and transmission electron microscopy (TEM). The SEM and TEM images reveal the sheet-like morphology of δ-MnO_2 nanoflakes, with lateral dimensions spanning from 20 to 200 nm (**Figure 1a,b**; Figure S1, Supporting Information). A high-resolution TEM (HR-TEM) image of the pristine δ-MnO_2 nanoflakes reveals its distinctive layered lattice structure, displaying an interplanar spacing of 0.715 nm corresponding to the (001) plane (Figure S1c, Supporting Information). In comparison, the V-δ-MnO_2 sample maintains the layered lattice structure, yet the interplanar spacing of the (001) plane increases to 0.73 nm, as shown in Figure 1c. Additionally, well-crystallized

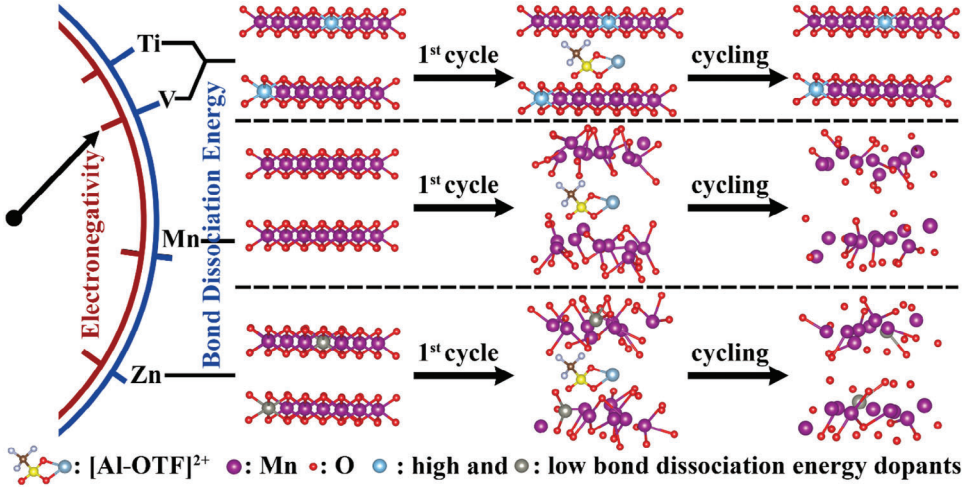

Scheme 1. Schematic illustration of the impact of heteroatoms doping on the electrochemical stability and performance of δ-MnO_2 cathodes during AAIBs cycling.

in-plane crystalline lattices of (110) and (200) are also observed and verified by the selected area electron diffraction (SAED) analysis shown in Figure 1c inset. Upon Ti and Zn doping, the nanostructures remain relatively consistent, accompanied by an increased interplanar spacing of 0.734 nm for Ti-δ-MnO_2 and 0.728 nm for Zn-δ-MnO_2, respectively (Figure S1f,i, Supporting Information). Figure S2 (Supporting Information) presents energy dispersive X-ray spectroscopy (EDS) elemental mappings of the doped δ-MnO_2 materials, illustrating consistent distributions of V, Ti, and Zn dopants throughout the materials. Additionally, the high-resolution EDS mappings of the V-δ-MnO_2 crystalline plane (Figure 1d–g), indexed from the (110) lattice fringe measuring 0.25 nm (Figure 1d), reveal isolated green dots (Figure 1f). This observation signifies the uniform atomic dispersion of V within the MnO_2 crystalline plane.

The X-ray diffraction (XRD) pattern presented in Figure 1h displays the crystal structure of pristine δ-MnO_2, identified as the Birnessite phase (JCPDS No. 43–1456). The distinctive diffraction peaks observed at ≈12.5° and 25.0° correspond to the (001) and (002) planes, thus confirming the layered crystalline structure. According to the Bragg equation, the *d*-spacing of the (001) plane is calculated to be 0.72 nm. V doping does not change the layered crystalline structure, but it causes the diffraction peaks to shift toward lower angles, indicating an expanded interplanar spacing of 0.73 nm. The XRD patterns for Ti and Zn doped δ-MnO_2 nanoflakes exhibit similar peak-shifting behaviors (Figure S3, Supporting Information), with calculated interplanar spacing values of 0.74 and 0.73 nm, respectively, consistent with the HR-TEM observations. The slightly increased interlayer distance after doping implies weakened interactions between the adjacent δ-MnO_2 planes. Introducing dopants also causes peak broadening in XRD patterns, suggesting a reduced average thickness of δ-MnO_2 nanoflakes. By analyzing the full width at half maximum (FWHM) values of (001) peaks, the thickness of pristine δ-MnO_2 is determined to be 18.85 nm, while V-δ-MnO_2, Ti-δ-MnO_2, and Zn-δ-MnO_2 show decreased thickness of 14.06, 13.76, and 14.75 nm, respectively (Table S1, Supporting Information).

X-ray photoelectron spectroscopy (XPS) analyses were conducted to investigate the chemical composition and bonding states of both pristine and doped δ-MnO_2 materials. The survey scanning spectra in Figure S4a (Supporting Information) can confirm the presence of Mn, O, and V/Ti/Zn in the respective materials. By analyzing the atomic ratio of each element, the doping content of V, Ti, and Zn was calculated to be 8.8%, 10.8%, and 11.6%, respectively (Table S2, Supporting Information). In the high-resolution Mn spectrum of pure δ-MnO_2 (Figure 1i), two distinct peaks at ≈654 and 642.3 eV in the Mn 2p spectra correspond to Mn $2p_{1/2}$ and Mn $2p_{3/2}$, respectively. The binding energies of the Mn 2p peaks for the doped δ-MnO_2 samples are shifted to lower positions compared to those of pristine δ-MnO_2 (Figure 1i; Figure S4b, Supporting Information), indicating a slight decrease in the mean oxidation states of Mn after doping.[9,27] The valence states of the dopants are also determined by their high-resolution XPS spectra shown in Figure 1i and Figure S4c,d (Supporting Information). The V 2p spectrum displays two characteristic peaks centered at 517.0 and 524.7 eV, assigned to $2p_{3/2}$ and $2p_{1/2}$ of V^{5+} species. The Ti $2p_{3/2}$ and $2p_{1/2}$ peaks at 458.4 and 464.1 eV suggest the formation of Ti^{4+}—O bonds, while the Zn $2p_{3/2}$ and $2p_{1/2}$ peaks at 1022.3 and 1045.3 eV imply the formation of Zn^{2+}—O bonds.

Collectively, the material characterizations confirmed the layered crystalline structures with wide interlayer spaces of the synthesized pristine and doped δ-MnO_2 nanoflakes. The selective introductions of dopants, including V, Ti, and Zn, have been successfully achieved within the δ-MnO_2 crystal planes, exhibiting uniform distributions in the lattice planes. The expanded interplanar distance and the decreased nanoflake thickness of δ-MnO_2 after introducing these dopants would alleviate stress during the reversible ion intercalation and de-intercalation processes, underscoring the structural benefit for the doped δ-MnO_2 materials as high-performance AAIB cathode candidates. The slight decrease of Mn mean oxidation states in doped δ-MnO_2 would also lead to the deformation of the initial Mn—O bond structure to mitigate the severe Jahn-Teller distortion during battery cycling.

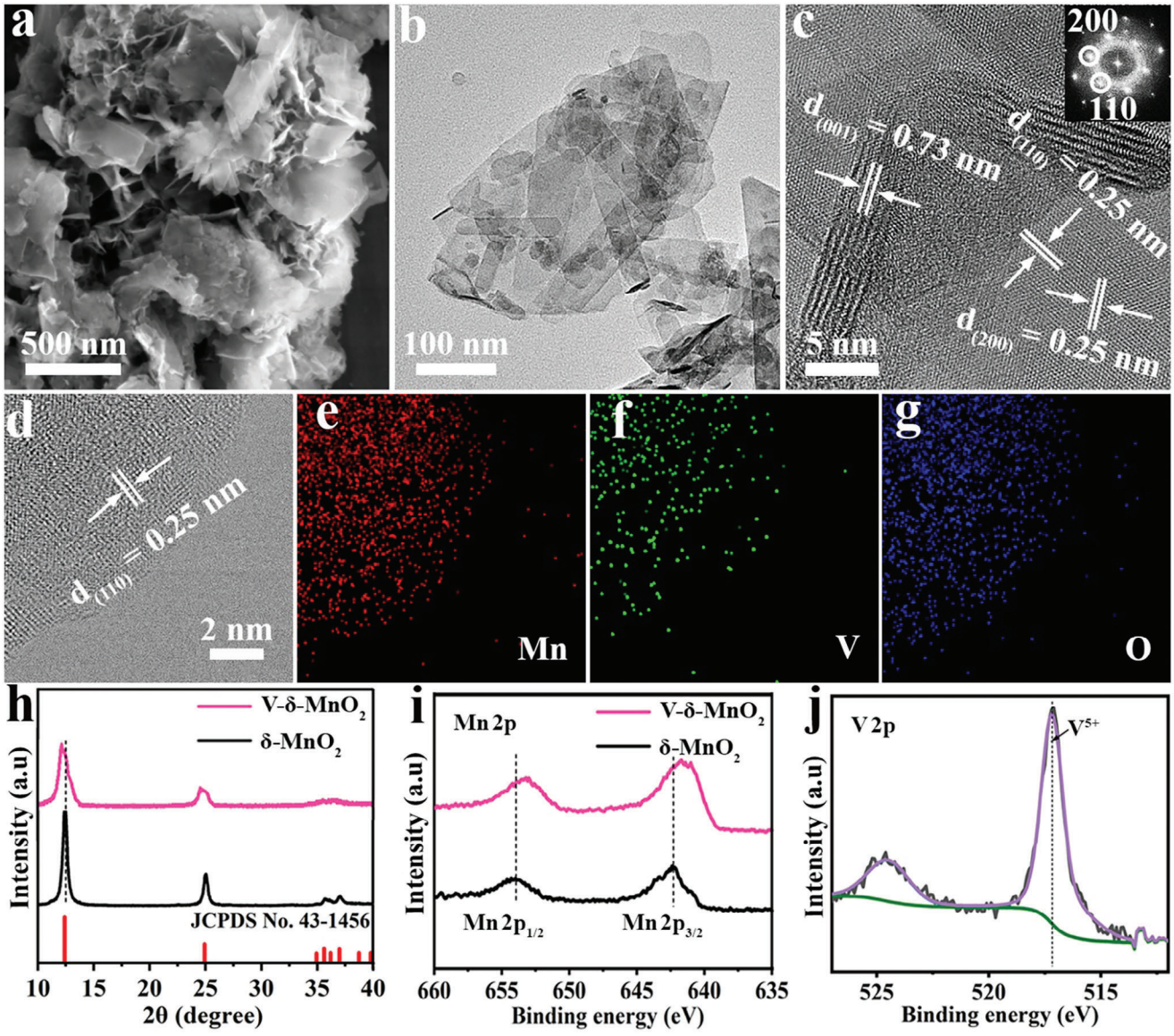

Figure 1. Material characterizations. a) SEM, b) TEM, and c) HR-TEM and SAED (inset) images of V-δ-MnO_2 nanoflakes. d–g) HR-TEM EDS elemental mapping of V-δ-MnO_2 crystalline plane. h) XRD patterns and i) Mn 2p XPS spectra of δ-MnO_2 and V-δ-MnO_2. j) V 2p XPS spectra of V-δ-MnO_2.

2.2. First-Principles Calculations

To explore the doping effect on the structural stability and ion storage property of δ-MnO_2, first-principles calculations were performed based on the density functional theory (DFT) (details can be found in the experimental section). Computational simulation of the structures of pristine and doped δ-MnO_2 materials validates the increased average Mn—O bond lengths post-doping (**Figure 2a**; Table S3, Supporting Information). More importantly, we assessed the structural stability of doped δ-MnO_2 through computational calculation of the cohesive energy (E_{Coh}) in a 3 × 3 × 1 supercell by **Equation 1**:

$$E_{Coh} = ((18 - x)\,\mu_{Mn} + 36\mu_O + x\mu_{Metal} - E_{MnO2})/54 \quad (1)$$

where x represents the number of doped metal atoms in the supercell (x = 0 or 2), E_{MnO2} is the total energy of the pure/doped δ-MnO_2 bilayer, and μ_{Mn}, μ_O and μm_{etal} denote the chemical potentials of Mn, O, and doped metal atoms, respectively. The potentials of metal atoms were determined based on the averaged energy of their corresponding stable crystal structures. Figure 2a shows the calculated E_{Coh} values of V-δ-MnO_2, Ti-δ-MnO_2, Zn-δ-MnO_2, and pristine δ-MnO_2. Ti-δ-MnO_2 presents the highest E_{Coh} of 1.695 eV, followed by V-δ-MnO_2 of 1.591, both surpassing the value of raw δ-MnO_2 (1.567 eV), while Zn-δ-MnO_2 exhibits the lowest E_{Coh} of 1.435 eV among all the materials. These calculated E_{Coh} values align well with metal—O bond dissociation energies, where higher cohesive energy signifies greater stability.[28,29] This suggests the feasibility of introducing high bond dissociation energy dopants as "oxygen binders" into δ-MnO_2

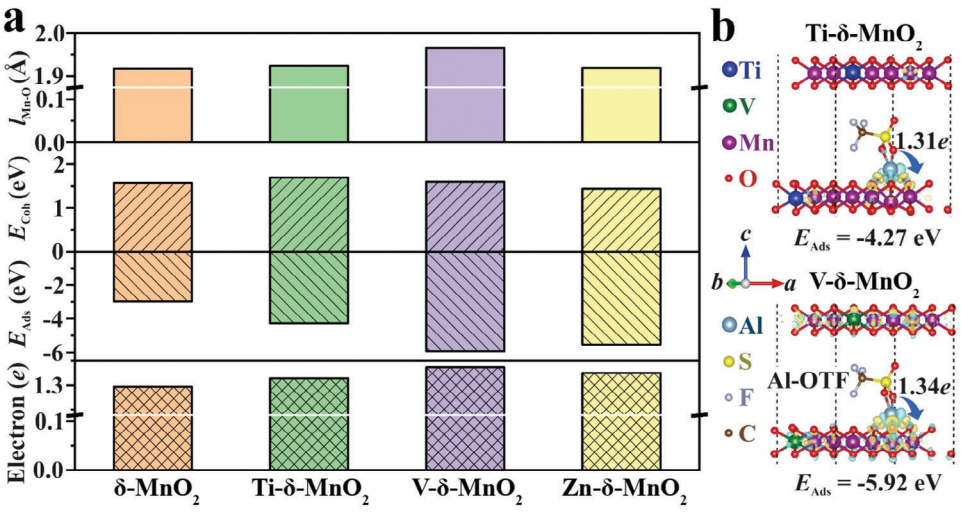

Figure 2. DFT calculations. a) Averaged bond length ($l_{Mn\text{-}O}$) for Mn—O, cohesive energy (E_{Coh}), adsorption energy (E_{Ads}) of Al-OTF and transferred electrons between metal (Ti, Vand Zn) doped δ-MnO_2 and Al-OTF, respectively. b) The charge density difference (iso-value of 0.01 e Å^{-3}) of Ti-δ-MnO_2 and V-δ-MnO_2 with Al-OTF intercalation, respectively. The yellow and cyan areas represent electron accumulation and depletion, respectively. The corresponding adsorption energy for Al-OTF is marked below each configuration.

frameworks to enhance their stabilities for high-performance AAIB cathodes.

Computational studies were conducted to investigate pristine and doped δ-MnO_2 cathodes at the intercalation state, aiming to understand the interactions between charge carriers and the δ-MnO_2 lattice. The adsorption energy (E_{Ads}) of intercalated δ-MnO_2 was calculated using a $3 \times 3 \times 1$ δ-MnO_2 bilayer unit with the insertion of one aluminum trifluoromethanesulfonate complex cation ([Al-OTF]$^{2+}$) per unit.[30] The equation (**Equation 2**) for determining E_{Ads} is as follows:

$$E_{Ads} = E_{MnO2-Al} - E_{MnO2} - \mu_{Al-OTF} \quad (2)$$

where $E_{MnO2\text{-}Al}$ represents the total energy of the bilayer after [Al-OTF]$^{2+}$ intercalation, E_{MnO2} is the total energy of the pristine/doped δ-MnO_2 bilayer, and $\mu A_{l\text{-}OTF}$ is the energy of the [Al-OTF]$^{2+}$ complex cation. The calculated E_{Ads} results and typical intercalated structures are presented in Figure 2a,b. Doped δ-MnO_2 materials exhibit significantly more negative E_{Ads} values compared to pristine δ-MnO_2 (Table S3, Supporting Information), indicating a more energetically favorable insertion of [Al-OTF]$^{2+}$ ions after doping. Specifically, V-δ-MnO_2 and Zn-δ-MnO_2 show similar E_{Ads} values of −5.92 and −5.55 eV, both lower than that of Ti-δ-MnO_2 (−4.27 eV). This difference can be attributed to the higher electronegativity of V (1.63) and Zn (1.65) compared to Mn (1.55) and Ti (1.54), as well as their aliovalent natures.

These factors promote the activity and electron mobility of oxygen sites and enhance the interaction with [Al-OTF]$^{2+}$ ions, which can be further validated by the increased transferred electrons between [Al-OTF]$^{2+}$ and MnO_2 layers in V-δ-MnO_2 and Zn-δ-MnO_2 over both Ti-δ-MnO_2 and pure δ-MnO_2 (Figure 2a; Table S3, Supporting Information). While the enhanced interaction benefits the attraction of [Al-OTF]$^{2+}$ ions for high-capacity δ-MnO_2 cathodes, it can also lead to structural perturbations during ion diffusion within the interlayers, which would be detrimental to Zn-δ-MnO_2 with an inferior E_{Coh}, to other δ-MnO_2 materials. Combining the DFT calculations of both E_{Coh} and E_{Ads}, the computational simulations indicate the promising potential of V-δ-MnO_2 as a high-performance cathode for AAIBs.

2.3. Electrochemical Performances of Pristine and Doped δ-MnO_2

The cathode performances of pristine and doped δ-MnO_2 were assessed in coin-cells utilizing aqueous Al(OTF)$_3$ solutions (2.0 mol L^{-1}) as the electrolyte and Al alloy foils as the anode (see details in the experimental section). In **Figure 3a**, the initial cycle's galvanostatic charge and discharge curves for the four δ-MnO_2 cathodes, measured at a current density of 200 mA g^{-1}, are presented. The selected voltage range for these tests spanned from 0.1 to 1.65 V. All four δ-MnO_2 cathodes exhibit distinct voltage plateaus during both charge and discharge steps. Most of the discharge capacities are delivered above 1.0 V, consistent with the cyclic voltammetry (CV) analysis results (Figure S5, Supporting Information) and characteristic behavior of δ-MnO_2 cathodes in AAIBs.[10,13,31,32] V-δ-MnO_2 demonstrates the highest specific discharge capacity of 518 mAh g^{-1}, surpassing Ti-δ-MnO_2 (481 mAh g^{-1}), Zn-δ-MnO_2 (432 mAh g^{-1}), and pristine δ-MnO_2 (472 mAh g^{-1}). V-δ-MnO_2 and Ti-δ-MnO_2 also exhibit elevated discharge voltage plateaus at 1.14 V, which is higher than those of Zn-δ-MnO_2 (1.09 V) and pristine δ-MnO_2 (1.06 V). In the second cycle, Ti-δ-MnO_2, Zn-δ-MnO_2, and pristine δ-MnO_2 cathodes experience a decrease in both discharge voltage and specific capacity (Figure S6, Supporting Information). Their discharge voltages decrease by 0.02, 0.1, and 0.05 V, respectively, and their specific capacities decrease by 9, 34, and 19 mAh g^{-1}, respectively. In contrast, V-δ-MnO_2 maintains its initial voltage profiles and specific discharge capacity, highlighting the advantage of high bond dissociation energy dopants in stabilizing δ-MnO_2 frameworks for enhanced cathode performance.

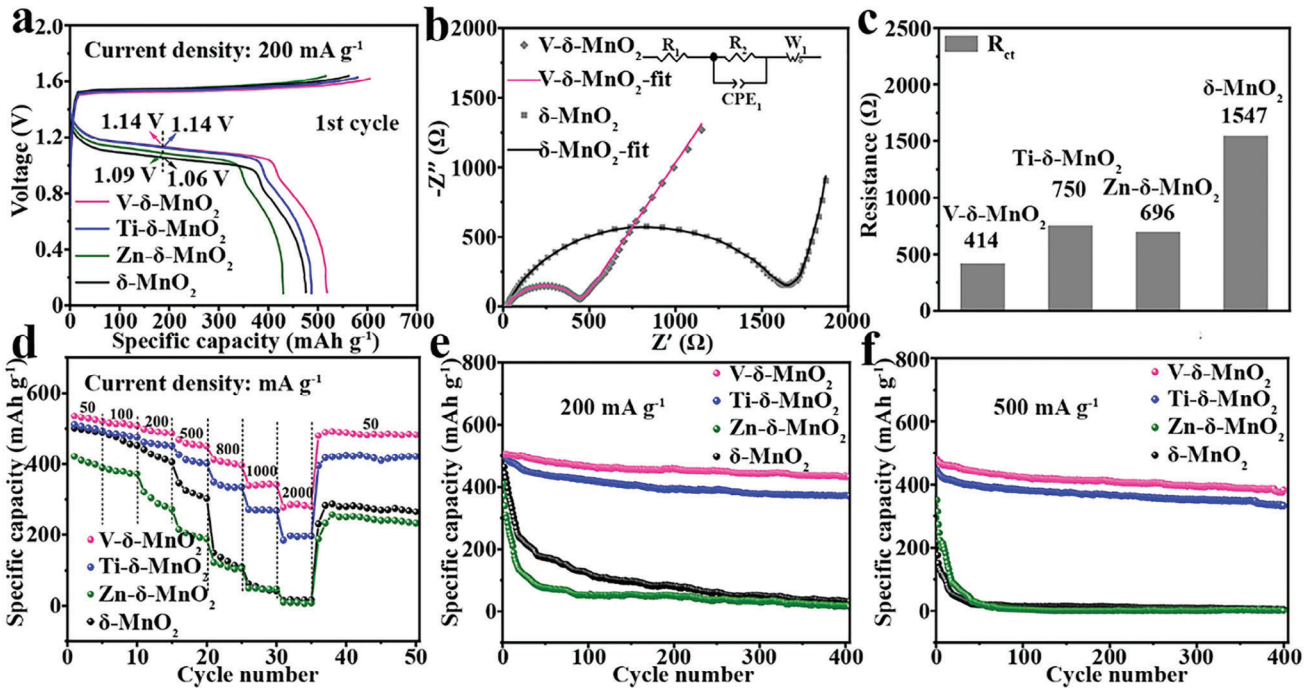

Figure 3. Electrochemical performances of pristine and doped δ-MnO_2 cathodes. a) Galvanostatic voltage profiles at the first cycle under a current density of 200 mA g^{-1}. b) Nyquist plots of V-δ-MnO_2 and δ-MnO_2 electrodes (Inset is the equivalent circuit). c) The charge transfer resistance of pristine and doped δ-MnO_2 cathodes. d) Rate performances of four δ-MnO_2 cathodes. e) and f) Cycling performances at 200 and 500 mA g^{-1}, respectively.

Electrochemical impedance spectroscopy (EIS) analyses were performed to investigate the electrochemical properties of δ-MnO_2 cathodes in AAIB systems. The Nyquist plots of four AAIB cells using V-δ-MnO_2, Ti-δ-MnO_2, Zn-δ-MnO_2, and pure δ-MnO_2 cathodes are shown in Figure 3b and Figure S7 (Supporting Information). The Nyquist plots, composed of semicircles in high frequency (f) region and sloping lines in low f area, can be fitted using the equivalent circuit (Figure 3b inset). In the circuit, R_1 is the electrolyte resistance and R_2 is the charge transfer resistance (R_{ct}). Based on the fitting results of the equivalent circuit, the determination of R_{ct} offers valuable insights into the electrochemical characteristics of the investigated cathodes. Figure 3c reveals that the R_{ct} fitting value of pristine δ-MnO_2 cathode is 1547 Ω. After doping, the R_{ct} significantly decreases, with the values for V-δ-MnO_2, Ti-δ-MnO_2, and Zn-δ-MnO_2 to be 414, 750, and 696 Ω, respectively. These changes occur because heterogeneous metal doping in δ-MnO_2 effectively increases the electrical conductivity and reduces the charge transfer resistance through the introduction of additional pathways for ion conduction and the creation of active sites.[12,33] The density of states (DOS) calculations in Figure S8 (Supporting Information) show that the pure δ-MnO_2 is a semiconductor with a band gap of ≈1.113 and 1.284 eV for spin-up and down channels. However, metallic states near the Fermi level exist in heterogeneous metals doped δ-MnO_2 materials, suggesting the enhancement of conductivity.[27,34]

The rate capacity and cycling performance of the doped and pure δ-MnO_2 cathodes were further assessed to evaluate their structural stability during battery operations. As shown in Figure 3d, V-δ-MnO_2 exhibits the most favorable rate performance, delivering specific capacities of 531, 515, 498, 468, 412, 339, and 285 mAh g^{-1} at current densities ranging from 50 to 2000 mA g^{-1}. In comparison, Ti-δ-MnO_2 shows relatively lower rate capacities at the corresponding current densities, maintaining a specific capacity of 197 mAh g^{-1} at 2000 mA g^{-1}. However, Zn-δ-MnO_2 and pristine δ-MnO_2 display significantly worse rate performances than V-δ-MnO_2 and Ti-δ-MnO_2. They experience substantial capacity decay as the current density increases, retaining only ≈10 mAh g^{-1} at 2000 mA g^{-1}. Furthermore, when the current density is reduced from 2000 to 50 mA g^{-1}, V-δ-MnO_2 and Ti-δ-MnO_2 almost fully recover their initial specific capacities. In contrast, Zn-δ-MnO_2 and pristine δ-MnO_2 can only restore ≈60% of their initial capacities. The voltage profiles of V-δ-MnO_2, Ti-δ-MnO_2, Zn-δ-MnO_2, and pristine δ-MnO_2 cathodes at selected current densities of 500, 800, 1000, and 2000 mA g^{-1} are also presented in Figure S9 (Supporting Information). V-δ-MnO_2 exhibits the highest discharge voltage plateaus at all four current densities, whereas Zn-δ-MnO_2 and pristine δ-MnO_2 experience severe voltage polarization at high currents.

The cycling stability of doped and pure δ-MnO_2 cathodes was measured at current densities of 200 and 500 mA g^{-1}, and the results are presented in Figure 3e,f. V-δ-MnO_2 exhibited the most stable cycling performance at both current densities, retaining high capacities of 436 mAh g^{-1} (86% at 200 mA g^{-1}) and 383 mAh g^{-1} (80% at 500 mA g^{-1}) after 400 cycles. The charge/discharge voltage profiles of V-δ-MnO_2 remained well-maintained throughout the cycling process (Figure S10, Supporting Information). Ti-δ-MnO_2 also exhibits good cycling stabilities for 400 cycles and maintains capacity retentions of 74% (372 mAh g^{-1}) and 75% (333 mAh g^{-1}) at 200 and 500 mA g^{-1}. In contrast, the capacities of Zn-δ-MnO_2 and pure δ-MnO_2 rapidly

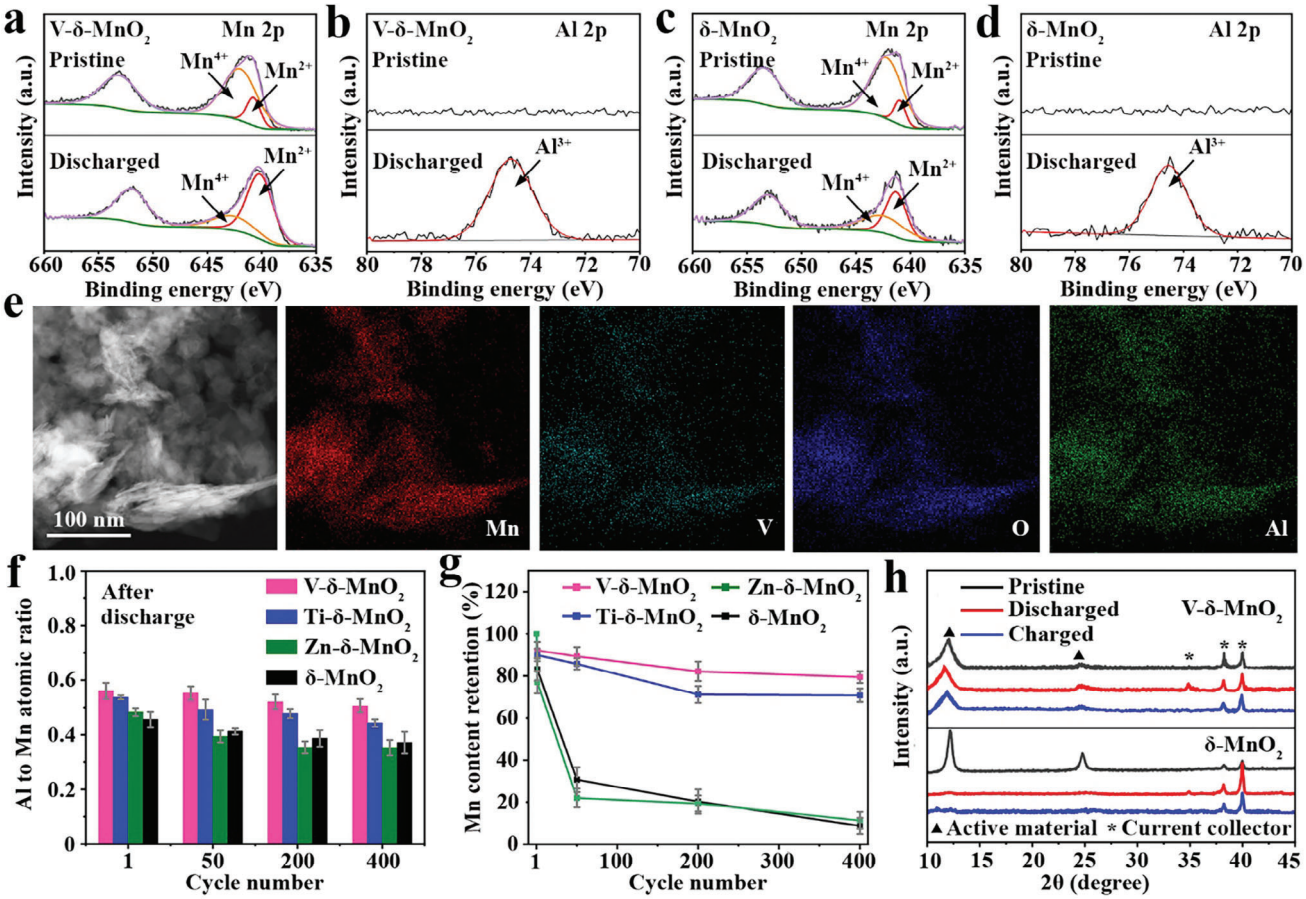

Figure 4. Composition and structural characterizations of δ-MnO_2 cathodes. a) and b) are the Mn 2p and Al 2p XPS spectra of V-δ-MnO_2 cathodes in the pristine and discharged states. c) and d) are the Mn 2p and Al 2p XPS spectra of pure δ-MnO_2 cathodes in the pristine and discharged states. e) The element distribution in V-δ-MnO_2 after discharging. f) The atomic ratios of Al to Mn in δ-MnO_2 cathodes after discharging at different cycles. g) Mn content in δ-MnO_2 cathodes at different cycles. h) XRD patterns for V-δ-MnO_2 and δ-MnO_2 electrodes at different states. The active material represents V-δ-MnO_2 and δ-MnO_2 in the electrodes. The current collector is titanium metal foil.

declined within the initial 50 cycles and eventually reached negligible values after 400 cycles for both current densities of 200 and 500 mA g^{-1}. The coulombic efficiencies of doped and pure δ-MnO_2 cathodes during the cycling tests were also recorded (Figure S11, Supporting Information). V-δ-MnO_2 and Ti-δ-MnO_2 both exhibit higher and more stable coulombic efficiencies compared to Zn-δ-MnO_2 and pure δ-MnO_2 over 400 cycles. The cycling and rate performance measurements clearly demonstrate the outstanding properties of the V-δ-MnO_2 cathode, surpassing other δ-MnO_2 cathodes and the reported cathode materials for AAIBs (Table S4, Supporting Information).[10,12–14,17,30–32,35–39] These results highlight the significantly improved cycling and rate performances of V-δ-MnO_2 and Ti-δ-MnO_2 compared to pristine δ-MnO_2, emphasizing the advantages of introducing high bond dissociation energy dopants to strengthen the δ-MnO_2 frameworks, thus enhancing their structural stabilities. Conversely, Zn doping leads to the formation of Zn—O bonds with inferior bond dissociation energy compared to Mn—O, weakening the cohesive energy of δ-MnO_2. Consequently, Zn-δ-MnO_2 exhibits the worst electrochemical performances among the doped and pure δ-MnO_2 cathodes.

To further understand the impact of different dopants on the stability and electrochemical performance of δ-MnO_2 cathodes, the chemical composition and structural evolution of doped and pristine δ-MnO_2 were investigated. The XPS analyses of four δ-MnO_2 electrodes before and after the first cycle discharging at 200 mA g^{-1} were presented in **Figures** 4a–d and S12a–d (Supporting Information). The deconvoluted Mn $2p_{3/2}$ peaks of the V-δ-MnO_2 electrode (Figure 4a) demonstrate that Mn is predominantly present as Mn^{4+} species and upon discharging, a pronounced reduction of Mn^{4+} to Mn^{2+} can be observed. The XPS spectra of V, Ti, and Zn in the doped δ-MnO_2 electrodes exhibit no significant valence change during battery charging and discharging (Figure S13, Supporting Information). This observation suggests that the dopants are not directly involved in the electrochemical reactions, and the cathode capacities are contributed by the redox reactions of Mn species. In the Al 2p XPS spectra, a new peak centered at 74.8 eV appears after discharging, corresponding to the simultaneous intercalation of Al ion species during the reduction of Mn^{4+} (Figure 4b). Similar phenomena can also be observed in Ti-δ-MnO_2, Zn-δ-MnO_2, and pure δ-MnO_2 electrodes. TEM-EDS elemental mappings of a typical V-δ-MnO_2

in the discharged state (Figure 4e) show uniform distributions of Mn, O, V, and Al throughout the specimen, verifying the intercalation of Al ion species during AAIB discharging, which is consistent with previous reports of δ-MnO_2 cathode reactions.[12,14]

The XPS element analyses of discharged cathodes throughout 400 cycles at 200 mA g^{-1} (Figure 4f) provide further confirmation of the incorporation of Al^{3+} species in δ-MnO_2 electrodes. Among the four cathodes, V-δ-MnO_2 exhibits the highest Al to Mn ratios, and Ti-δ-MnO_2 displays slightly lower values, which align with the long-cycling capacities as shown in Figure 3e. In contrast, for Zn-δ-MnO_2 and pure δ-MnO_2 cathodes, despite the notable Al to Mn ratios at 200 and 400 cycles, their capacities have decayed to almost negligible levels, indicating severe Mn leaching during battery cycling. We further employed the inductively coupled plasma-optical emission spectroscopy (ICP-OES) technique to monitor the Mn dissolution behavior of doped and pure δ-MnO_2 cathodes. After 400 cycles, the V-δ-MnO_2 cathode retains 80% of the Mn, outperforming the Ti-δ-MnO_2 cathode with a retention rate of 72% (Figure 4g). In comparison, both δ-MnO_2 and Zn-δ-MnO_2 cathodes demonstrate fairly low Mn retentions, measuring below 20%. These results suggest that the doping of V/Ti effectively suppresses the Mn dissolution from δ-MnO_2 during cycling.

Figure 4h presents the XRD patterns of the electrodes at the initial, discharged, and charged stages in the first cycle. In the initial state of the V-δ-MnO_2 electrode, diffraction peaks corresponding to both δ-MnO_2 nanoflakes and the titanium current collector (Figure S14, Supporting Information) can be observed. Even after the first discharging and charging processes, comparable peaks are still evident, indicating the preservation of the layered V-δ-MnO_2 despite the insertion and extraction of charge carriers. In contrast, it becomes challenging to observe diffraction peaks of the layered structure in pure δ-MnO_2 electrode after the first cycle discharge, and this effect remains irreversible after charging, suggesting the disruption of the layered structure. The layered structure of the Ti-δ-MnO_2 cathode is also well-preserved after the first cycle charge and discharge, as shown in Figure S15 (Supporting Information). However, in Zn-δ-MnO_2 cathodes, the diffraction peaks of δ-MnO_2 become almost indiscernible after the first cycle discharge and charge. Notably, even after undergoing 400 cycles, the V-δ-MnO_2 cathode continues to exhibit identifiable diffraction peaks corresponding to its layered structure (Figures S16 and S17, Supporting Information). These observations provide strong evidence for the enhanced structural stability of V-δ-MnO_2 and Ti-δ-MnO_2 to withstand the reversible intercalation and de-intercalation of Al ions with high ionic potential. This validates the hypothesis of introducing high bond dissociation energy dopants, such as Ti—O and V—O, as "oxygen binders" to strengthen δ-MnO_2 frameworks, verifying the results of our computational studies. The stabilized δ-MnO_2 materials effectively preserve active Mn species in the cathodes, improve conductivity, and eventually deliver high capacities with prolonged cycling life in AAIBs.

3. Conclusion

In summary, we have synthesized heterogeneous metals (V, Ti, and Zn) doped δ-MnO_2 nanoflakes and studied the impact of different dopants on the stability of δ-MnO_2 cathodes in AAIBs. Through a combination of computational simulations and experimental characterizations, it has been revealed that metal dopants forming strong bonds with oxygen can effectively enhance the cohesive energy of δ-MnO_2 lattices and result in improved structural stability against the reversible intercalation of high ionic potential Al ions. Electrochemical testing demonstrated that V-δ-MnO_2 and Ti-δ-MnO_2, with high energy V—O and Ti—O bonds, exhibit stable cycling performance for 400 cycles and remarkable rate capabilities, outperforming Zn-δ-MnO_2 and pure δ-MnO_2. Further comparative analysis between V-δ-MnO_2 and Ti-δ-MnO_2 indicates that the higher electronegativity and the aliovalent nature of V contribute to an enhanced affinity for Al ion species, resulting in improved specific capacities at various current densities. This work presents a new strategy to stabilize manganese oxide-based cathode materials for AAIB and holds promise for influencing cathode design in other aqueous multivalent metal-ion batteries.

4. Experimental Section

Preparation of δ-MnO_2-Based Cathode Materials: δ-MnO_2 was synthesized using hydrothermal procedures. During the process, a solution containing 4 mL of 0.3 M $Mn(NO_3)_2$ was mixed with 16 mL of 0.6 M NaOH and 2 M H_2O_2 (30 wt.%) and vigorously stirred for 30 min at room temperature, resulting in the formation of a precipitate. The precipitate was then dissolved in 30 mL of 2 M NaOH solution and transferred to a 100 mL Teflon-lined stainless-steel autoclave. The autoclave was heated at 150 °C for 20 h. After cooling to room temperature, the product was centrifuged, washed with deionized water three times, and dried at 60 °C overnight to ensure its purity and remove any residual impurities. V/Ti/Zn-MnO_2 was prepared using the same method but with the inclusion of dopants in the precursor solution. The dopants, namely NH_4VO_3, $TiOSO_4$, and $Zn(NO_3)_2$ $6H_2O$, were added to the solution in a doping metal-to-Mn atomic ratio of 3:10.

Computational Method: First-principles calculations were performed based on the density functional theory (DFT), as implemented in the Vienna ab initio simulation package (VASP).[40,41] The exchange-correlation energy of the ions was described by the Perdew–Burke–Ernzerhof functional within the framework of the generalized gradient approximation (GGA-PBE) method.[42] A $3 \times 3 \times 1$ Gamma-Centred k-grid was adopted to simulate the first-Brillouin zone in the reciprocal space, due to large lattice parameters in the $3 \times 3 \times 1$ supercell of MnO_2. The kinetic cut-off energy was set to be 500 eV, while the criterion for convergence was set to be 10^{-4} and 0.01 eV $Å^{-1}$ for the energy and force on each atom, respectively. The DFT-D3 correction was adopted for the weak interlayer van der Waals interactions.[43]

Supporting Information

Supporting Information is available from the Wiley Online Library or from the author.

Acknowledgements

The authors acknowledge the financial support from the Australian Research Council, the Queensland Government, and the University of Queensland. This work used the Queensland node of the NCRIS-enabled Australian National Fabrication Facility (ANFF). The authors also acknowledge the facilities and the scientific and technical assistance of the Australian Microscopy & Microanalysis Research Facility at the Centre for Microscopy and Microanalysis, The University of Queensland.

Open access publishing facilitated by The University of Queensland, as part of the Wiley - The University of Queensland agreement via the Council of Australian University Librarians.

Conflict of Interest

The authors declare no conflict of interest.

Data Availability Statement

The data that support the findings of this study are available from the corresponding author upon reasonable request.

Keywords

aqueous aluminium-ion batteries, cathodes, heteroatoms doping, manganese oxides

Received: March 1, 2024
Published online: March 15, 2024

[1] B. Sambandam, V. Mathew, S. Kim, S. Lee, S. Kim, J. Y. Hwang, H. J. Fan, J. Kim, *Chem* **2022**, *8*, 924.
[2] X. F. Shen, X. N. Wang, Y. R. Zhou, Y. H. Shi, L. M. Zhao, H. H. Jin, J. T. Di, Q. W. Li, *Adv. Funct. Mater.* **2021**, *31*, 9.
[3] C. Zhong, B. Liu, J. Ding, X. R. Liu, Y. W. Zhong, Y. Li, C. B. Sun, X. P. Han, Y. D. Deng, N. Q. Zhao, W. B. Hu, *Nat. Energy* **2020**, *5*, 440.
[4] D. H. Wang, L. F. Wang, G. J. Liang, H. F. Li, Z. X. Liu, Z. J. Tang, J. B. Liang, C. Y. Zhi, *ACS Nano* **2019**, *13*, 10643.
[5] P. Almodovar, D. A. Giraldo, J. Chancon, I. Alvarez-Serrano, M. L. Lopez, *ChemElectroChem* **2020**, *7*, 2102.
[6] X. Xiao, Z. W. Zhang, Y. C. Wu, J. W. Xu, X. Gao, R. Xu, W. X. Huang, Y. S. Ye, S. T. Oyakhire, P. Zhang, B. L. Chen, E. Cevik, S. M. Asiri, A. Bozkurt, K. Amine, Y. Cui, *Adv. Mater.* **2023**, *35*, 2211555.
[7] J. Ji, H. Z. Wan, B. Zhang, C. Wang, Y. Gan, Q. Y. Tan, N. Z. Wang, J. Yao, Z. H. Zheng, P. Liang, J. Zhang, H. B. Wang, L. Tao, Y. Wang, D. L. Chao, H. Wang, *Adv. Energy Mater.* **2021**, *11*, 10.
[8] S. Q. Liu, B. Y. Wang, X. Zhang, S. Zhao, Z. H. Zhang, H. J. Yu, *Matter.* **2021**, *4*, 1511.
[9] X. Y. Xia, Y. J. Zhao, Y. Zhao, M. G. Xu, W. Liu, X. M. Sun, *Nano Res.* **2023**, *16*, 2511.
[10] S. M. He, J. Wang, X. Zhang, J. Z. Chen, Z. C. Wang, T. T. Yang, Z. W. Liu, Y. Liang, B. Y. Wang, S. Q. Liu, L. Q. Zhang, J. Y. Huang, J. Huang, L. A. O'Dell, H. J. Yu, *Adv. Funct. Mater.* **2019**, *29*, 1905228.
[11] B. Zhou, Z. Y. Zhou, B. Li, Z. L. Qu, Q. Song, C. M. Zhang, Z. Y. Jiang, Y. Ding, *J. Phys. D-Appl. Phys.* **2021**, *54*, 12.
[12] J. L. Yang, W. B. Gong, F. X. Geng, *Adv. Funct. Mater.* **2023**, *33*, 2301202.
[13] C. S. Yan, C. Lv, L. G. Wang, W. Cui, L. Y. Zhang, K. N. Dinh, H. T. Tan, C. Wu, T. P. Wu, Y. Ren, J. Q. Chen, Z. Liu, M. Srinivasan, X. H. Rui, Q. Y. Yan, G. H. Yu, *J. Am. Chem. Soc.* **2020**, *142*, 15295.
[14] C. Wu, S. C. Gu, Q. H. Zhang, Y. Bai, M. Li, Y. F. Yuan, H. L. Wang, X. Y. Liu, Y. X. Yuan, N. Zhu, F. Wu, H. Li, L. Gu, J. Lu, *Nat. Commun.* **2019**, *10*, 73.
[15] G. J. Li, L. Sun, S. L. Zhang, C. F. Zhang, H. Y. Jin, K. Davey, G. M. Liang, S. L. Liu, J. F. Mao, Z. P. Guo, *Adv. Funct. Mater.* **2023**, *34*, 2301291.
[16] B. Yong, D. T. Ma, Y. Y. Wang, H. W. Mi, C. X. He, P. X. Zhang, *Adv. Energy Mater.* **2020**, *10*, 38.
[17] Q. Ran, H. Shi, H. Meng, S. P. Zeng, W. B. Wan, W. Zhang, Z. Wen, X. Y. Lang, Q. Jiang, *Nat. Commun.* **2022**, *13*, 576.
[18] Q. X. Xie, G. Cheng, T. Xue, L. H. Huang, S. H. Chen, Y. Sun, M. Sun, H. Z. Wang, L. Yu, *Mater. Today Energy* **2022**, *24*, 10.
[19] D. A. Kitchaev, S. T. Dacek, W. H. Sun, G. Ceder, *J. Am. Chem. Soc.* **2017**, *139*, 2672.
[20] G. Tyler, *Sci. Total Environ.* **2004**, *329*, 231.
[21] J. Lee, S. Lee, M. M. Islam, J. Jang, *Adv. Eng. Mater.* **2022**, *24*, 8.
[22] S. Aikawa, T. Nabatame, K. Tsukagoshi, *Appl. Phys. Lett.* **2013**, *103*, 5.
[23] S. Parthiban, J. Y. Kwon, *J. Mater. Chem. C* **2015**, *3*, 1661.
[24] Y. D. Zhang, J. D. Liu, W. C. Xu, Y. Lu, H. Ma, F. Y. Cheng, J. Chen, *J. Power Sources* **2022**, *535*, 231445.
[25] G. M. Liang, E. Olsson, J. S. Zou, Z. B. Wu, J. X. Li, C. Z. Lu, A. M. D'Angelo, B. Johannessen, L. Thomsen, B. Cowie, V. K. Peterson, Q. Cai, W. K. Pang, Z. P. Guo, *Angew. Chem., Int. Ed.* **2022**, *61*, 11.
[26] J. A. Dean, *Lange's handbook of chemistry*, McGraw-Hill, New York, USA **1999**.
[27] S. Y. Yao, R. Zhao, S. Y. Wang, Y. X. Zhou, R. C. Liu, L. Y. Hu, A. Q. Zhang, R. Yang, X. Liu, Z. N. Fu, D. W. Wang, Z. Y. Yang, Y. M. Yan, *Chem. Eng. J.* **2022**, *429*, 9.
[28] Z. Chen, G. F. Li, H. Z. Zheng, X. Y. Shu, J. P. Zou, P. Peng, *Appl. Surf. Sci.* **2017**, *420*, 205.
[29] A. Boisset, L. Athouël, J. Jacquemin, P. Porion, T. Brousse, M. Anouti, *J. Phys. Chem. C* **2013**, *117*, 7408.
[30] Y. X. Li, L. J. Liu, Y. Lu, R. J. Shi, Y. L. Ma, Z. H. Yan, K. Zhang, J. Chen, *Adv. Funct. Mater.* **2021**, *31*, 2102063.
[31] Q. Zhao, M. J. Zachman, W. I. Al Sadat, J. X. Zheng, L. F. Kourkoutis, L. Archer, *Sci. Adv.* **2018**, *4*, eaau813.
[32] C. S. Yan, C. D. Lv, B. E. Jia, L. X. Zhong, X. Cao, X. L. Guo, H. J. Liu, W. J. Xu, D. B. Liu, L. Yang, J. W. Liu, H. H. Hng, W. Chen, L. Song, S. Z. Li, Z. Liu, Q. Y. Yan, G. H. Yu, *J. Am. Chem. Soc.* **2022**, *144*, 11444.
[33] Y. F. Zhao, J. Q. Zhang, W. J. Wu, X. Guo, P. Xiong, H. Liu, G. X. Wang, *Nano Energy* **2018**, *54*, 129.
[34] B. R. Li, Y. F. Chu, B. Xie, Y. C. Sun, L. Zhang, H. M. Zhao, L. Zhao, P. F. Liu, J. J. He, *J. Mater. Chem. A* **2023**, *11*, 2133.
[35] J. C. Chen, Q. N. Zhu, L. Jiang, R. Y. Liu, Y. Yang, M. Y. Tang, J. W. Wang, H. Wang, L. Guo, *Angew. Chem., Int. Ed.* **2021**, *60*, 5794.
[36] Q. Zhao, L. J. Liu, J. F. Yin, J. X. Zheng, D. H. Zhang, J. Chen, L. A. Archer, *Angew. Chem., Int. Ed.* **2020**, *59*, 3048.
[37] S. Liu, J. J. Hu, N. F. Yan, G. L. Pan, G. R. Li, X. P. Gao, *Energy Environ. Sci.* **2012**, *5*, 9743.
[38] R. F. Bai, J. Yang, G. J. Li, J. Y. Luo, W. J. Tang, *Energy Storage Mater.* **2021**, *41*, 41.
[39] X. J. Li, Y. C. Tang, C. A. Li, H. M. Lv, H. D. Fan, W. L. Wang, T. H. Cai, Y. P. Cui, W. Xing, Z. F. Yan, C. Y. Zhi, H. F. Li, *J. Mater. Chem. A* **2022**, *10*, 4739.
[40] G. Kresse, J. Furthmuller, *Comput. Mater. Sci.* **1996**, *6*, 15.
[41] G. Kresse, J. Furthmuller, *Phys. Rev. B* **1996**, *54*, 11169.
[42] J. P. Perdew, K. Burke, M. Ernzerhof, *Phys. Rev. Lett.* **1996**, *77*, 3865.
[43] S. Grimme, J. Antony, S. Ehrlich, H. Krieg, *J. Chem. Phys.* **2010**, *132*, 19.